Journal of Materials Chemistry C

# Devising Novel Methods for the Controlled Synthesis with Morphology and Size Control of Scintillator Materials



| | |
|---|---|
| Journal: | *Journal of Materials Chemistry C* |
| Manuscript ID | TC-ART-03-2020-001211.R1 |
| Article Type: | Paper |
| Date Submitted by the Author: | 06-May-2020 |
| Complete List of Authors: | Hurley, Nathaniel ; Stony Brook University, Chemistry<br>Moretti, Federico; Lawrence Berkeley National Laboratory, 1 Cyclotron road, Berkeley, CA 94720, USA<br>Yan, Hanfei; Brookhaven National Laboratory,<br>Bourret, Edith; Lawrence Berkeley National Laboratory<br>Chu, Yong; Brookhaven National Laboratory, National Synchrotron Light Source II<br>Wong, Stanislaus; Stony Brook University, |
| | |

# Devising Novel Methods for the Controlled Synthesis with Morphology and Size Control of Scintillator Materials

Nathaniel Hurley,[1] Federico Moretti,[2] Hanfei Yan,[3] Edith Bourret-Courchesne,[2]

Yong S. Chu,[3] and Stanislaus S. Wong[1,*]

Email: stanislaus.wong@stonybrook.edu; sswong@bnl.gov

[1]Department of Chemistry, State University of New York at Stony Brook, Stony Brook, NY 11794-3400

[2]Materials Sciences Division, Lawrence Berkeley National Laboratory, Berkeley, California 94720

[3]National Synchrotron Light Source II, Building 743, Brookhaven National Laboratory, Upton, NY 11973

*To whom correspondence should be addressed.

**Abstract**

Nanoscale scintillators represent an important class of materials underlying the functioning of high resolution, high 'light yield' radiation detection equipment, applicable for medicine in addition to security and environmental monitoring. This current study has focused on the controlled synthesis of $Cs_2ZnX_4$ (X = Cl, Br) not only due to its very fast and promising radioluminescence decay time but also because no reliable synthesis protocols have been reported for producing nanoscale motifs of this material, to date. Solution-based methods can be used to synthesize products, possessing different, discrete morphologies with the ability to dictate particle size and shape. Specifically, we have demonstrated that a hot injection technique can be used to fabricate nanoscale rods and plates. Using this method, we systematically studied the effect of varying reaction variables, such as (i) reaction temperature, (ii) surfactants, and (iii) reaction time. As synthesized nanorods of $Cs_2ZnCl_4$ possessed lengths of 101.3 ± 24.4 nm with widths of 17.3 ± 4.5 nm, whereas $Cs_2ZnBr_4$ created under identical conditions were characterized by lengths of 206 ± 50 nm and widths of 26.7 ± 12.6 nm. Ligand assisted coprecipitation (LARP) was used to produce the corresponding micron-sized particles. Under these conditions, we successfully synthesized spindles and spherical particles of $Cs_2ZnCl_4$ with sizes of 1.58 ± 0.16 μm and 1.03 ± 0.34 μm, respectively, whereas plates of $Cs_2ZnBr_4$ were prepared with average sizes of 0.76 ± 0.21 μm. High resolution synchrotron mapping, using the hard X-ray nanoprobe at NSLS II, was used to confirm the expected spatial distribution of Cs, Zn, and Cl within the as-produced crystals. Nanorods of $Cs_2ZnCl_4$ and $Cs_2ZnBr_4$ were subsequently tested for scintillation light yield and decay times. Preliminary results showed that $Cs_2ZnCl_4$ maintained a light yield of 100-300 photons/MeV with a fast decay component of 2.6 ns. The $Cs_2ZnBr_4$ analogue did not give rise to any perceptible scintillation emission.

## 1. Introduction

High energy radiation detection is used in the fields of security,[1] environmental monitoring,[2] medicine,[3] as well as exploratory instrumental techniques in physics and chemistry.[4] For these techniques to work, the detected radiation must first be converted into a form, that will not necessarily damage the detectors. Scintillators represent a viable option for this type of conversion as they work by transforming ionizing radiation into low energy photons. The current work will focus on the synthesis and characterization of novel scintillator materials.

The purpose of this study therefore is (i) to create novel morphologically well-defined nanoscale formulations of a class of scintillator materials that are known to possess a very fast scintillation decay time and a high energy resolution in bulk, (ii) to carefully explore reaction conditions to develop a simple and generalizable solution-based methodology to control morphology and monodispersity of these scintillating materials, and (iii) to provide for preliminary data in terms of understanding relevant structure-property correlations within these systems. To address these issues, the model material chosen for this effort is $Cs_2ZnX_4$ (X = Cl, Br), which has shown scintillation properties in bulk form with a 2.2 mm sheet exhibiting an 80% detection efficiency, a 1.8 ns decay time, and a light yield of 630 photons/MeV.[5-7]

What is therefore novel about our study can be summarized, as follows. (i) Neither nanoscale nor micron-sized crystalline motifs of either $Cs_2ZnCl_4$ or $Cs_2ZnBr_4$ materials have ever been previously generated. Based upon a survey of the prior literature, there have not been any evident solution-based procedures that have provided for rational morphology and chemical control with respect to $Cs_2ZnX_4$ (X = Cl, Br). Moreover, neither SEM nor TEM characterization data have been systematically reported for these materials. (ii) We have used reasonably mild and controllable solution-based synthesis methods to determine the size, chemical composition,

and morphology of these materials. (iii) We have studied the growth mechanism of the crystals. (iv) We have collected preliminary photoluminescence and radioluminescence data of as-produced materials. Finally, (v) we have acquired X-ray fluorescence imaging (XRF) elemental mapping data, which have not been previously reported for $Cs_2ZnCl_4$.

In particular, single crystals of $Cs_2ZnCl_4$ can be used as scintillators for biomedical applications, as they exhibit core valence luminescence (CVL). CVL denotes a very fast luminescence process with decay times on the order of 0.6 to 3.0 ns.[8] Indeed, scintillators are intriguing for a wide range of feasible medical applications, such as but not limited to fluorescent labels[9] and light-emitting components, associated with photodynamic therapies (PDT).[10-21] In the context of imaging, it is known that traditional labels, such as organic molecules and quantum dots, often suffer from photobleaching. Moreover, the capabilities of fluorescent labels are limited by the penetration depth of visible, infrared, and ultraviolet light, normally used to activate fluorescence. In effect, scintillators can potentially overcome all of these aforementioned limitations, because (i) they are normally activated by X-rays, which can give rise to deep penetration throughout biological tissue, and because (ii) they are relatively 'immune' to photobleaching. Our nanoscale scintillator materials possess promising properties as a viable class of structures for bio-labeling, due to (a) relatively fast decay times which should allow for higher-resolution imaging and (b) our ability to tune morphology between zero-dimensional particles versus anisotropic one-dimensional (1D) rods.

In particular, PDT may be used as a viable modality with which to treat cancers and other illnesses, by using photons from an external source in order to photochemically activate and induce the formation of reactive oxygen species (ROS). These short-lived oxygen radicals are toxic, and may lead to cell death.[10] In the context of PDT, scintillators are especially promising,

because they can be locally activated by X-rays, which enable a deeper, targeted penetrating ability as opposed to using either visible or UV light.[22] Hence, in terms of theranostics, nanoscale scintillators can potentially be used to locally image, target, and treat specific cells in a directed manner as opposed to indiscriminately damaging large swaths of healthy cells in the process. Their efficacy is therefore a function of (i) our capability to control morphology coupled with (ii) the ability to tailor the toxicity of these scintillator materials, in general.

In general, $Cs_2ZnCl_4$ and $Cs_2ZnBr_4$ are typical examples of a class of ternary halide compounds with an $A_2BX_4$ composition in which "A" is a large cation, "B" is a small cation ion, and the "X" is a halide anion. These materials are characterized by an orthorhombic space group of *Pnma*. This crystal structure possesses a tetrahedral geometric configuration around the central zinc atom. Figure 1 highlights a 'ball-and-stick' schematic of the $Cs_2ZnCl_4$ crystal structure. Materials, such as $Cs_2ZnCl_4$ and $Cs_2ZnBr_4$, are fundamentally interesting, since they combine high atomic number elements, which are desirable for scintillation, in the context of structures that are known to possess favorable CVL properties.

Herein, our study resolves to achieve the following goals. (i) Develop materials as potential labeling entities, that can lead to higher resolution X-ray imaging capabilities for applications in medicine and security. (ii) Lower the high cost of generating scintillation materials by using relatively mild solution-based techniques for their reliable production.

To emphasize the necessity of our study, it is worth pointing out that previously reported synthesis methods (discussed in more detail in the Supplementary Information section), used to make these types of scintillator materials, are relatively limited in scope. These reported procedures include (i) a vertical Bridgman-Stockbarger technique,[7, 23] (ii) a 'slow evaporation' process,[24-26] and (iii) the Czochralski method.[27] However, these traditional production protocols

tend to be limited by issues, such as the need for high temperatures, expensive specialized equipment, and/or exceedingly long reaction times.

In the current report, we have employed solution-based methods to *synthesize different nanoscale morphologies* of $Cs_2ZnCl_4$ and $Cs_2ZnBr_4$. We have created nanoscale motifs of both $Cs_2ZnCl_4$ and $Cs_2ZnBr_4$, using a modified version of an established hot injection method.[28, 29] This procedure utilizes a 'mild-to-moderate' heating regime between 50°C to 200°C, coupled with surfactants to control size and morphology. As-prepared crystals are not air-sensitive, and the reactions can be carried out entirely under ambient pressure conditions. Moreover, these reactions can be performed at more moderate temperatures as compared with analogous processes, such as either Bridgman-Stockbarger or Czochralski procedures. In addition, the protocol uses lower purity precursors as compared with the aforementioned bulk methods. For example, crystals of our samples can be generated using different lower-purity precursors, including cesium acetate and cesium halide. Furthermore, the solution-based method that we have devised herein can be performed more quickly, since the reaction takes ~20 minutes to complete. Finally, our devised procedure does not require the use of any specialized and/or costly equipment, such as either quartz ampoules or a vertical heating apparatus in order to attain the high temperatures, characteristic of the Bridgman-Stockbarger method.

To synthesize micron-sized particles, we have utilized a 'ligand-assisted re-precipitation' (LARP) method. LARP has previously been used to generate quantum dots of halide crystals.[30] This procedure can therefore induce 'morphology control' in terms of creating various controllable sizes (i.e., micron to sub-micron scale) and shapes of micron to sub-micron scale geometrically well-defined crystals of $Cs_2ZnCl_4$ and $Cs_2ZnBr_4$ at room temperature. LARP is performed entirely under ambient conditions and requires no heating. The crystallization process

occurs essentially instantaneously, when a 'good' solvent containing the precursors is injected into a 'poor' solvent in which the precursors are insoluble; this overall procedure initiates precipitation and stimulates crystallization, because the desired products end up precipitating and 'crashing' out of solution. We should mention that both the hot injection method and LARP are easily scalable simply by increasing the reaction vessel size and the quantity of precursors.

## 2. Experimental

### 2.1. Materials

All chemicals were used without further purification. Specifically, 2-propanol (99.5%) and zinc bromide ($ZnBr_2$, 99.9%) were purchased from Beantown Chemical. Cesium bromide (CsBr, 99.9%), cesium chloride (CsCl, 99.999%), N,N-dimethylformamide (DMF, 99.7+%), n-hexane (95+%), cyclohexane (99%), toluene (99.5%), and dodecanoic acid (99.9%) were acquired from Alfa Aesar. Triethylene glycol (TEG) was obtained from Kodak Chemicals. Zinc chloride ($ZnCl_2$), oleic acid (OA, 90%), nonylamine (NLA, 98%), trimethoxysilane (TMOS), and cesium acetate, respectively, were procured from Aldrich Chemicals. N-butylamine (BLA, 99%) was purchased from Arcos Organics. Tetradecane was acquired from the Phillips Petroleum Company.

### 2.2. Synthesis

#### 2.2.1. Synthesis of nano-scale $Cs_2ZnCl_4$

Precursor cesium-acid complexes were made by using a previously reported method.[28] Simply, 0.471 g of cesium acetate was mixed with 13.5 ml octadecene, 1.25 ml oleic acid, and 1.25 ml oleylamine in a 20 mL vial. Under vigorous stirring, the solution was heated to 110°C for 30 mins. Then the solution was heated to 150°C, until the cesium acetate was fully dissolved.

The solution was then either heated or cooled to the proper injection temperature. Cesium-acid complex solutions were prepared in fresh batches, daily.

Nanoscale particles were prepared using a modified hot injection method.[29] In a typical synthesis of $Cs_2ZnCl_4$ nanorods, 20 mL of octadecene was mixed with 0.1 g $ZnCl_2$, 2 mL oleic acid, and 2 mL oleylamine within a 50 mL, 3-necked round bottom flask. The reaction vessel was then heated to 150°C. Any remaining undissolved $ZnCl_2$ was allowed to dissolve, before proceeding. At this juncture, 2 mL of the previously prepared cesium-acid complex precursor solution was heated to at 150°C and then rapidly injected. The resulting solution was allowed to stir at 150°C for an additional 20 minutes. We isolated our sample upon rapid cooling in an ice bath, followed by washing of the solution with hexane for 3 times at 9000 rpm for 10 minutes. The bromide samples were analogously prepared, but in the presence of an excess of $ZnBr_2$, a condition which was necessary to inhibit the precipitation of an excess of CsBr impurities.

### 2.2.2. Synthesis of micron-scale $Cs_2ZnCl_4$ and $Cs_2ZnBr_4$

In a typical synthesis to produce the desired compounds, either a combination of 0.15 g of $ZnCl_2$ and 0.122 g CsCl (in a 1.5: 1 molar ratio, since excess $ZnCl_2$ was needed to dissolve all of the CsCl) or an analogous blend of 0.165 g of $ZnBr_2$ and 0.155 g CsBr (1: 1 molar ratio) was dissolved in 4 ml DMF under vigorous stirring within a 20 mL vial. Upon dissolution, 1.166 mL OA was added, followed by 0.408 mL TEG. The precursor solution was allowed to stir for 5 minutes. After stirring, 200 μL of solution was pipetted into a larger quantity of 10 mL of toluene in the presence of stirring. Precipitation occurred essentially instantly, and the solution was allowed to stir for an additional minute. The solutions were centrifuged twice with toluene, twice with isopropanol (so as to remove remaining zinc complexes), and once with hexane (to get rid of any remnant isopropanol) at 9000 rpm for 3 minutes per wash.

### 2.2.3. Synthesis of bulk $Cs_2ZnCl_4$

Bulk $Cs_2ZnCl_4$ was grown using a previously reported slow evaporation method. In a typical synthesis, 0.100 g $ZnCl_2$ and 0.247 g CsCl were added to a 20 ml vial and then dissolved with 5 ml of DI water. This resulted in a clear solution. The vial was then covered in parafilm, punctured with several holes to allow for evaporation. This solution was left undisturbed for several days, until millimeter sized crystals were grown. Individual crystals were removed and ground in a mortar and pestle to obtain the desired powder.

## 2.3. Characterization

### 2.3.1. X-ray diffraction (XRD)

Powder X-ray diffraction measurements were obtained on a Rigaku MiniFlex 600 benchtop diffractometer. Indeed, powder XRD was used to enable both chemical composition and phase identification. Samples were prepared by dispersing the powder in hexane; 2-propanol was used for micron sized samples. The dispersion was then drop cast onto a zero background holder (MTI Corporation, Zero diffraction plate for XRD, B-doped, *p*-type Si, with measurements of 23.6 mm in diameter by 2 mm in thickness). Relevant data were collected from 10 to 80° at a rate of 10 degrees per minute.

### 2.3.2. Scanning electron microscopy (SEM)

The morphology and size of $Cs_2ZnCl_4$ and $Cs_2ZnBr_4$ nanostructures were probed using a JEOL JSM-7600F field emission SEM instrument. Relevant images were taken with an accelerating voltage of 5 kV at a working distance of 3.5 to 4.5 mm, with an SEI detector. SEM grids for analysis were prepared by dispersing fixed quantities of as-generated samples in hexane and drop casting these onto underlying silicon (Si) wafers.

### 2.3.3. Transmission electron microscopy (TEM)

The morphology and size of $Cs_2ZnCl_4$ nanostructures were probed using a JEOL 1400 TEM instrument. Lower resolution TEM images were acquired using an accelerating voltage of 80 kV, since the use of higher voltages would presumably damage the sample and degrade the desired morphology. Samples were subsequently drop cast onto 3 mm lacey carbon-coated copper grids, prior to analysis.

**2.3.4. X-ray Fluorescence Imaging**

2D Scanning X-ray fluorescence imaging with a minimum beam size of 12 nm and an energy range of 12-16 keV was used to collect high-resolution element mapping data of $Cs_2ZnCl_4$. This work was done at the National Synchrotron Light Source II (NSLS-2) 3-ID HXN (Hard X-ray nanoprobe) beamline.

**2.3.5. Radioluminescence / Photoluminescence**

Room temperature radioluminescence (RL) spectra have been obtained using a copper rotating anode X-ray generator (50 kV, 60 mA, Brüker) and a spectraPro-2150i spectrometer (Acton Research Corp.), coupled to a PIXIS: 100B CCD (Princeton Instruments) apparatus. The same light detection set-up was also used to measure the photoluminescence (PL) signal, using a Xe lamp coupled to a monochromator (Acton) as the excitation source. Filters have been used to avoid the presence of higher diffraction orders emanating from the grating. All of the presented spectra have been corrected for not only instrument response but also light transport of the optical components.

Pulsed X-ray decays have been obtained with the time-correlated single photon counting technique using a custom-built system composed of an ultrafast Ti: sapphire laser, a light-excited X-ray tube (Hamamatsu N5084), and a multi-channel plate photomultiplier (Hamamatsu R3809U-50). The start and stop signal timing was obtained with an Ortec 9308 ps analyzer. The

overall instrument response function maintains a full width at half maximum of the order of 200 ps. No wavelength discrimination was used to select the light emitted by the samples.

In short, the light yield (LY) values reported in the paper are at best a rough approximation. To obtain these data, we compared the area under the radioluminescence curves of our samples with the one of a YAP: Ce powder we have normally used as a reference and set the latter to the usually accepted light yield value for YAP. We subsequently calculated the signal from the $Cs_2ZnBr_4$ sample as a simple ratio. The spectra are corrected, so these do take into consideration any variation, as a function of wavelength, of the system response. Nevertheless, what we have really measured is actually 'Light Output' as opposed to 'Light Yield', since our data were obtained with a steady state radiation source as opposed to a conventional radioactive gamma-source (e.g. $^{137}Cs$). Specifically, light yield and light output data are correlated, but might differ substantially in actual magnitude.

**3. Results and Discussion**

Our approach in this work has been to demonstrate chemical and physical morphological control over scintillator systems. Specifically, since there have not been any reports about nanoscale morphological control for $Cs_2ZnX_4$, herein, we have systematically investigated reaction conditions to determine their individual effects upon nanoparticle size and shape. In particular, we investigated the discrete effects of varying (i) reaction temperatures from 50°C to 200°C at intervals of 50°C, (ii) the presence/absence of amine and carboxylic acid-containing surfactants, and (iii) reaction times between 5 seconds and 60 minutes. To ensure that we were probing the effect of changing only one variable at a time, all of the other reaction conditions remaining invariant during these reactions. Specifically, reaction parameters kept constant across

the breadth of the reactions analyzed included the final volume, the concentration of precursor solutions, and the molar ratios of amines versus carboxylic acids, normally kept at a value of 1:1, except where changes were specifically noted. We proceed to address and probe the discrete effects of each of these variables in the context of $Cs_2ZnCl_4$ and $Cs_2ZnBr_4$ model systems.

### 3.1. Temperature (Hot Injection Method)

Reaction temperature affects many aspects of nanoparticle growth, including (i) kinetics, (ii) the solvation and dispersion of ligated precursors, and (iii) the strength of surfactant binding onto the crystal planes. As the temperature increases, the crystal growth rate increases, the diffusion rates of intermediate complexes go up, and the corresponding binding of surfactants is weakened.[31-33] The collective effects of these various conditions dictate the growth of crystals along various crystal facets. This growth can be observed during our trials, as we increased the temperature from 50°C to 200°C in increments of 50°C. The surfactants used were oleic acid and oleylamine, whose collective function was to control morphology by not only forming a confining soft template but also coordinating onto the crystal surface. The solvent 1-octadecene was also used, since it can solubilize both the surfactants and ligand-coated precursors. The only variable altered between reactions was the temperature itself.

#### 3.1.1. Effect of Varying Reaction Temperature on $Cs_2ZnCl_4$

As is apparent from our data, there is a clear transition from the formation of spherical particles (Figure 2A), with a size of 93.3 ± 9.9 nm, generated at a temperature of 50°C, to the production of nanorods, isolated at 150°C (Figure 2C), possessing average lengths of 101.3 ± 24.4 nm and widths of 17.3 ± 4.5 nm. Figure 2B highlights the presence of smaller, isotropically shaped nanoparticles (with an average size of 36.3 ± 10.9 nm), grown at a lower temperature, i.e. 100°C. The generation of relatively monodisperse spherical nanocrystals fabricated at low

temperatures implies a slow growth rate. Rounded particles, created under slow growth rates, are favored at low temperatures, because the surfactants in the reaction medium bind strongly, thereby stabilizing the facets and resulting in a relatively uniform, homogeneous growth process. At higher temperatures, the surfactants are bound less tightly, thereby allowing for 'anisotropic' growth along high energy facets in particular. Because crystal growth is highly dependent upon surface energy, lower-energy facets are more apt to terminate, due to comparatively slower growth conditions as opposed to those favoring high-energy facet formation.[31]

Upon comparing the rods grown at 150°C and 200°C (Figure 2D), it can be observed that the rods produced at the higher temperatures are larger and less uniform with average lengths of 239.6 ± 101.7 nm and average widths of 25.7 ± 4.6 nm. This scenario may be due to the fact that at higher temperatures, in general, precursor diffusion is more prevalent. Furthermore, uniform surfactant binding/attachment onto the growing facets is less likely, thereby favoring the creation of more polydisperse, more anisotropic, and hence, relatively less homogeneous features, such as plates. Over time, these constituent plate-like motifs end up elongating and stacking, thereby leading to a more polydisperse distributions of rods, characterized by large lengths and diameters. In effect, the postulated reduction in binding strength decreases the surfactants' ability to stabilize the growing facets, thereby reducing their ability to precisely control size and shape and ultimately leading to an overall decrease in uniformity noted.

Figure 3 indicates the presence of XRD patterns of the crystal, obtained at different temperatures. Peaks are indexed in SI Figure S1B. All of these data match the predicted $Cs_2ZnCl_4$ pattern and show phase purity. To emphasize the importance of size, the diffraction pattern for the sample generated at 100°C is notably broader and less defined as compared with the other patterns. This result was seen in different runs, meaning that these differences in the

observed patterns are caused by the crystals themselves. For instance, the broadened peaks within the measured pattern may be potentially ascribed to the smaller size of the particles. Nanoparticles with average diameters less than 100 nm tend to show significant peak broadening, due to their reduced crystallite size.[34] As such, the average size of 36.3 nm is sufficiently small enough to have yielded a noticeable peak broadening.

### 3.1.2. Effect of Varying Reaction Temperature on $Cs_2ZnBr_4$

The hot injection method was also able to produce the bromide analogue of the desired material, i.e. $Cs_2ZnBr_4$. An excess of $ZnBr_2$ was needed in order not only to ensure full reaction with all of the cesium ions but also to push the reaction equilibrium towards the formation of $Cs_2ZnBr_4$. It should be noted that in the absence of an excess of precursors, cesium bromide crystals with a cubic geometry dominate.

To probe the effect of temperature upon the growth of $Cs_2ZnBr_4$, the same temperature range was used, as with $Cs_2ZnCl_4$. To achieve comparable results between chloride and bromide analogues of this material, all of the samples were created with a 20 minute reaction time. All other reaction variables, except for temperature, were also kept constant between reactions. XRD data were used to confirm the chemical composition at each temperature, and these data suggested that pure $Cs_2ZnBr_4$ was synthesized at all of the reaction temperatures tested (Figure 4). TEM images providing insight into the growth of these nanomaterials at reaction temperatures between 50°C and 200°C for $Cs_2ZnBr_4$ are shown in Figure 5.

From these data, there is a clear morphological evolution from acicular particles grown at low temperature to the formation of rods produced at high temperature. At 50°C, acicular particles possessing an average size of 26.3 ± 5.4 nm were observed (Figure 5A). As with $Cs_2ZnCl_4$, we propose that this low temperature range is not sufficient to either weaken the

surfactant binding or stimulate the growth of high-energy facets. Because of this experimental hypothesis, particle growth is noticeably uniform along all of the planes.

At 100°C, square plates, characterized by an average size of 43.9 ± 10.4 nm and an average thickness of 4.6 ± 0.9 nm, begin to form (Figure 5B). At 150°C, 1D nanorods possessing average lengths, widths, and thicknesses of 206 ± 50 nm, 26.7 ± 12.6 nm, and 6.9 ± 1.2 nm, respectively, are created (Figure 5C). At 200°C, larger 1D nanorods with measured lengths and widths of 642 ± 334 nm and 40.7 ± 29.1 nm, respectively, are produced (Figure 5D). The morphological progression from plates generated at 100°C to rods developed at 150°C to very long rods synthesized at 200°C suggests that all else being equal, temperature maintains a direct correlation with particle growth. Specifically, as reaction temperature increases, the binding of the surfactants decreases, thereby allowing for the high energy planes to form and grow more rapidly with a concomitant increase in the polydispersity of the final products isolated. Furthermore, the temperature rise likely promotes the elongation and assembly of anisotropic constituent components, thereby accounting for the corresponding increase in rod thickness.

**3.2. Surfactants (Hot Injection)**

Surfactants control morphology by binding onto crystal facets and stabilizing them. This leads to either slower or faster growth along specific planes. Changing surfactants can correspondingly alter binding properties, and this can lead to the production of different morphologies. In order to understand the effect of different surfactants with respect to morphology control, a systematic study was performed by predictively changing and tuning the length of the nonpolar carbon tail on the acid and base surfactants. The surfactants are all variations of either fatty acids with different non-polar tail lengths or fatty amines with similar non-polar tails. A list of surfactants chosen along with their corresponding structures is presented

in SI Table S1. SI Table S2 contains a series of TEM images and corresponding measurements of all trials, wherein surfactant acid base pairs were changed.

### 3.2.1. Effect of Varying Surfactant on $Cs_2ZnCl_4$

Empirically, we have found that both acid and base surfactants are required to achieve morphology control. To determine why, we ran the reaction with only either acid or base. This current study was performed with oleic acid and oleylamine. SI Table S3 highlights all of the trials using different amounts of oleic acid and oleylamine. The reaction run in the absence of oleylamine was designated as OLA-free, and the subsequent reaction in the absence of oleic acid is labeled as OA-free. First, it must be noted that cesium acetate does not dissolve in the presence of oleylamine alone. Hence, the OA-free reaction did in fact contain a small amount of oleic acid, introduced from the injection of the cesium oleate precursor solution. We found that the OA-free reaction yielded irregularly shaped particles and rods possessing a large variety of sizes (Figure 6D). Specifically, the OLA-free reaction generated large textured spheres with an average size of 21.2 ± 4.9 μm (Figure 6C).

The corresponding XRD data suggests that the product of the OLA-free reaction consisted of pure $Cs_2ZnCl_4$, whereas the analogous product from the OA-free reaction was impure (SI Figure S2). We postulate that pure $Cs_2ZnCl_4$ crystals will grow in OLA-free conditions through direct interactions and combination of ions in solution. In effect, this cumulative set of results is consistent with the idea that the simultaneous presence of *both* acid and base surfactants is necessary to create isolated nanoscale particles of $Cs_2ZnCl_4$.

We also altered the chain length of the acid and base surfactants, since this parameter is known to impact particle growth and lead to the formation of different morphologies.[28, 33] As such, we systematically modified the composition of the basic amine surfactants from

nonylamine (a fatty amine with a 9-carbon tail) to oleylamine (an unsaturated fatty amine, characterized by a longer-chain, more hydrophobic 18 carbon tail). The reported results are associated with reactions run at 150°C to enable a more direct comparison with data on other reactions, run at the same temperature. The net result of these experiments with shortened basic surfactants involved the generation of rods with lengths of 68.7 ± 16.8 nm and widths of 30.6 ± 9.3 nm (Figure 6A). These dimensions are about 30% shorter and 40% wider than the analogous rods grown using OLA, a scenario which might have arisen from the ability of nonylamine to bind more strongly onto the growing particle surface, thereby resulting in a more restricted and spatially confined growth. Indeed, the shorter non-polar tail of the nonylamine may have rendered it less soluble in hydrophobic 1-octadecene. This situation would have caused nonylamine to have been less likely to diffuse and conversely, more likely to coordinate onto the charged ions of the growing crystalline lattice.

In another series of experiments, dodecanoic acid, a carboxylic acid with a 12-carbon alkane tail, was used instead of OA. This choice yielded similar results to that of nonylamine, with as-prepared rods characterized by lengths of 69.5 ± 13.0 nm and widths of 21.4 ± 2.5 nm (Figure 6B). These data also suggest that acid surfactants with shorter nonpolar tails likely bind more strongly onto the growing facets, thereby accounting for the shortened rods (Table S2).

Reducing the amount of oleylamine (i.e., to about 150 μL) resulted in the formation of nanocubes with an average size of 24.5 ± 4.1 nm. Little change in morphology was noted as the corresponding amount of OLA was increased to 350 μL (SI Figure S3A, B). By contrast, increasing the amounts of oleylamine and oleic acid by as much as 3 fold led to the formation of large flat rods measuring 252.7 ± 84.1 nm in length, 27.0 ± 3.3 nm in width, and 9.9 ± 1.5 nm in thickness (SI Figure S3C). Indeed, all else being equal, increasing the surfactant concentration

resulted in the generation of nanorods with similar widths and thicknesses as those created at 150°C, but at the same time, with significantly increased lengths.

### 3.3. Reaction Time (Hot Injection)

#### 3.3.1. Effect of Varying Reaction Time on $Cs_2ZnCl_4$

Optimizing the correct growth time was critical to achieving proper control over particle size and morphology. Most of the literature concerned hot injection techniques suggests that the reaction needs to be quenched within 5-30 seconds so as to generate either nanoparticles or quantum dots. However, we found that the most uniform and homogeneous particle morphologies could be isolated after 20 min of reaction. Indeed, lowering the reaction time to 5 seconds at different temperatures resulted in the formation of irregular nanoparticles in very low yields. Conversely, samples obtained after 60 minutes were characterized by an evident degradation in morphology as compared with those samples prepared after a reaction interval of 20 minutes. Collectively, all of these results imply that a sufficient reaction time within a relatively narrow reaction window was necessary for engineering complete particle growth beyond mere nucleation. As mentioned, the sample morphology was noted to be irregular after either overly long or conversely, much shortened reaction times. SI Table S4 provides data on all of the measurements, associated reaction conditions, and corresponding TEM images for all trials attempted for the production of $Cs_2ZnCl_4$ with respect to the idea of varying reaction times at different reaction temperatures.

These data trends were consistent for samples, acquired at 100°C, 150°C, and 200°C, respectively (SI Figures S4A-F). Because of the apparent lack of both compositional and morphological dependence upon reaction time, we did not pursue additional trials with $Cs_2ZnCl_4$.

#### 3.3.2. Effect of Varying Reaction Time on $Cs_2ZnBr_4$

Interestingly, altering the chemical composition of the crystal from chloride to bromide resulted in more significant morphology changes with respect to reaction time. In fact, this chemical composition also evinced less susceptibility to degradation, as the reaction time was increased. The corresponding results are shown in Supplementary Figure S5. At 50°C, the acicular particles remained fairly unchanged from a size of 34.9 ± 8.8 nm, produced at 5 seconds, but increased to 34.2 ± 9.9 nm after 1 hour of reaction (SI Figure S5A, B). These results agree with the idea that at low temperatures, the surfactants bind sufficiently strongly to inhibit growth. SI Table S5 lists associated measurements, reaction conditions, and TEM images, with respect to the concept of changing reaction times at different temperatures, for all trials done for $Cs_2ZnBr_4$.

At 100°C, we observed a progression from the formation of acicular particles possessing an average size of 23.3 ± 7.6 nm grown after 5 seconds to the fabrication of square plates with an average width of 43.9 ± 10.4 nm and an average thickness of 4.6 ± 0.9 nm, as the reaction time was increased to 1 hour (SI Figure S5C, D). We perceived little difference in terms of plate size and shape beyond a reaction time of 20 minutes and 60 minutes, respectively.

At 150°C, square plates grew after 5 seconds to an average size of 36.1 ± 11.4 nm and an average thickness of 4.3 ± 0.8 nm. After 1 hour, the plates evolved into flat rods with average dimensions associated with lengths of 217 ± 56 nm, widths of 30.4 ± 9.3 nm, and thicknesses of 6.4 ± 1.3 nm (SI Figure S5E, F). Moreover, not surprisingly, rods manufactured after 1 hour were slightly larger than those analogously grown at 20 minutes.

At 200°C, rods were found to have increased in dimension at all reaction times. In effect, these products progressed in size from the formation of short rods with average lengths and widths of 118 ± 33 nm and 22.1 ± 4.3 nm respectively, produced at 5 seconds to the production

of comparatively larger rods with average lengths and widths of 2.5 ± 32.66 μm and 0.3 ± 0.1 μm respectively, created after 60 minutes (SI Figure S5G, H).

### 3.4. Mechanistic Insights into Morphology control of $Cs_2ZnX_4$ with Hot Injection

The growth mechanism for $Cs_2ZnX_4$ plates likely follows a previously reported process for the formation of ionic cesium halide ternary compounds.[35, 36] These reports use a similar hot injection procedure with oleic acid and oleylamine as coordinating surfactants within a nonpolar medium of octadecene. The reaction mechanism has two key components, starting with the formation of $Zn^0$ seeds. The seeds are initially formed in a solution containing $ZnX_2$ (X = Cl, Br), oleic acid, oleylamine, and octadecene as the solvent. $ZnX_2$ precursors dissolve, as the mixture is heated to 110°C. To isolate the seed particles, the solution was heated from 110°C to 150°C and immediately quenched. Images of the seeds are shown in Figure 7. The use of $ZnCl_2$ and $ZnBr_2$ precursors yielded seeds with average sizes of 2.80 ± 0.66 nm and 1.65 ± 0.30 nm, respectively (Figure 7A, B). Because of this finding, we should emphasize that the first step of the reaction process was likely identical for both $Cs_2ZnBr_4$ and $Cs_2ZnCl_4$. Chemically speaking $Zn^0$ seeds were created by reduction from $Zn^{2+}$ ions in a process likely mediated by oleylamine, which can serve in the roles of both a reducing and a capping agent.[37] It is noteworthy that the isolated $Zn^0$ seeds particles did not appear to be impacted by electron beam degradation, when performing electron microcopy, whereas the $Cs_2ZnX_4$ crystals were more notably affected.

To visualize the effect of seed particles upon the initial growth process, the reaction was quenched immediately after the injection of Cs oleate. Subsequently, both the supernatant and precipitate were collected and imaged using TEM. Figure 7C and D highlight the seed particles isolated from the supernatant for $Cs_2ZnCl_4$ and $Cs_2ZnBr_4$, respectively. Scattered precursor seed particles are clearly visible in Figure 7E, which reveals that round $Cs_2ZnCl_4$ nanoparticles were

produced after immediate quenching from 150°C. By contrast, more rectangular motifs of $Cs_2ZnBr_4$ (Figure 7F) were generated in the relative absence of such seed species. This observation suggests that the intrinsic morphology of the seed particles in and of themselves does not necessarily dictate the ultimate product shape. Rather, growth beyond the initial nucleation process is likely controlled by the presence of oleic acid and oleylamine surfactants, which collectively act as a soft template within the solution with which to 'modulate' the surface energy of the growing crystal facets. In this manner, constituent components of anisotropic morphologies, such as rods[38] and plates, may form, and ultimately aggregate and elongate into larger assemblies of plates and rods. We summarize our findings within Figure 8, which presents a concise mechanistic flow chart associated with the seed-mediated growth of $Cs_2ZnX_4$.

### 3.5. LARP Method for $Cs_2ZnCl_4$ and $Cs_2ZnBr_4$

In separate experiments, we also tried the LARP method to attempt to control morphology. This procedure simply involves the dissolution of precursors in a 'good' solvent (in this case, either DMF, water, or triethylene glycol), adding in an acid surfactant such as oleic acid, and then precipitating the product by dropping in a small aliquot of a non-polar, 'poor' solvent, such as toluene. The LARP method works, because the crystal precursors are super-saturated, when added to the poor solvent. Because of this fact, they crystallize immediately. The surfactants control this crystallization process by stabilizing the growth and formation within a soft template framework. As mentioned, this soft template limits aggregation and restricts particle growth.[39] Because we have found that the identities of polar good solvents, non-polar poor solvents, and surfactants can all individually yield a noticeable effect upon crystal morphology, many different combinations have been attempted.

Hence, in the design of this synthesis, the 'good' solvents attempted included water, DMF, and triethylene glycol. As mentioned, polar 'good' solvents are needed to dissolve not only the CsX and $ZnX_2$ ($X = Cl^-, Br^-, I^-$) precursors but also the oleic acid surfactant. 'Poor' solvents needed to be not only nonpolar enough to induce precipitation but also sufficiently miscible within the good solvent. Water was chosen as the first 'good' solvent, because it is non-toxic, abundant, and can easily solubilize the cesium and zinc salts; however, oleic acid is not water soluble. To overcome this obstacle and ensure precursor solubility, small amounts of isopropanol were initially added to the water, until oleic acid became sufficiently miscible, but not in such large amounts so as to encourage crystal precipitation. Subsequently, $Cs_2ZnCl_4$ was precipitated using larger aliquots of isopropanol, functioning as a 'poor' solvent.

Nonetheless, we found that water could not be used as a 'good' solvent for the bromide and iodide analogues, since no miscible 'poor' solvent could be found to induce precipitation of the desired product. We therefore changed the solvent to DMF, as this was able to solubilize not only the precursors but also the surfactant, i.e. oleic acid. Moreover, DMF was miscible with a wider variety of non-polar solvents other than water, including various alcohols, toluene, chloroform, and dichloromethane. Using this set of experimental conditions, both chemical compositions of $Cs_2ZnCl_4$ and $Cs_2ZnBr_4$ could be readily obtained. It should be said that no good solvent/ poor solvent combination could precipitate $Cs_2ZnI_4$; only CsI would precipitate (see SI Table S6). SI Tables S7 and S8 list all of the reactions run for the LARP method along with the observed, corresponding results for both $Cs_2ZnCl_4$ and $Cs_2ZnBr_4$.

From our cumulative data, we found that the LARP method was not quite as effective as hot injection in terms of precise control over sample size distribution, uniformity, and shape. Specifically, we ended up fabricating plate-like and particulate motifs on the scale of microns.

Typical morphologies of $Cs_2ZnCl_4$, created using the LARP method, are presented in Figure 5. In effect, we were able to generate spindles characterized by sizes of 1.58 ± 0.16 μm, using triethylene glycol as the solvent and oleic acid as the surfactant (Figure 9A). Moreover, we synthesized particles of $Cs_2ZnCl_4$, possessing a size of 1.03 ± 0.34 μm, generated in the presence of DMF, oleic acid, and triethylene glycol (Figure 9B).

In parallel experiments, $Cs_2ZnBr_4$ plates were fabricated with DMF, oleic acid, and triethylene glycol and were characterized by measured sizes of 0.76 ± 0.21 μm (Figure 9C). Based on our many runs, it was determined that the LARP method could only reliably and reproducibly turn out reasonably large particles with fairly irregular morphologies.

Nevertheless, correct chemical compositions were corroborated by XRD data (SI Figure S6) for both samples containing $Cs_2ZnCl_4$ particles and spindles. Similarly, the XRD pattern of $Cs_2ZnBr_4$ plates also evinced the expected chemical composition, especially when compared with published spectra (SI Figure S7). Indexed diffraction patterns for both $Cs_2ZnBr_4$ and $Cs_2ZnCl_4$ samples are provided in SI Figure S1A and B respectively. SI Figure S8 indicates that the correct chemical composition was isolated for bulk $Cs_2ZnCl_4$, created by slow evaporation.

### 3.6. Spectroscopic Studies

#### 3.6.1. X-ray fluorescence imaging

XRF data were collected for as-prepared $Cs_2ZnCl_4$ particles, generated by the LARP method. Figure 10A highlights the elemental mapping distribution of these samples. Specifically, Figure 10A-D presents data on the spatial localization of individual elements of chlorine, cesium, and zinc. From these results, we observed a relatively homogeneous distribution of each of these elements, a finding which correlates well with predictions, based on the crystal structure. Indeed, the phase contrast (Figure 10E) and the differential phase contract (Figure 10F) images are

consistent with a reasonably uniform phase distribution, suggesting the relative stability of our samples towards the incident radiation. Indeed, no phase separation appears to have been induced by the data collection process in accordance with our expectation that a scintillator material should be sufficiently robust enough so as not to undergo decomposition upon exposure to high-energy X-ray irradiation.

**3.6.2. Spectroscopic Studies - Photoluminescence**

Coupled photoluminescence excitation and emission maps of $Cs_2ZnCl_4$ and for $Cs_2ZnBr_4$ are reported in Figure S9A and B. The PL and PLE spectra obtained from the maps are reported for selected excitation and emission wavelengths of $Cs_2ZnCl_4$ and for $Cs_2ZnBr_4$ (Figure S9C, D). The PL decay time for the $Cs_2ZnCl_4$ nanorods measured 3.66 ± 0.07 ns. For the $Cs_2ZnCl_4$ spindles, $Cs_2ZnCl_4$ particles, and $Cs_2ZnBr_4$ plates, the associated corresponding decay times were noted to be 3.13 ± 0.07 ns, 2.74 ± 0.06 ns, and 2.40 ± 0.08 ns, respectively.

Both $Cs_2ZnCl_4$ and $Cs_2ZnBr_4$ nanorod samples show a relatively simple emission centered in the blue-violet region of the spectrum with a slight blue shift of the emission from the $Cl^-$ to the $Br^-$ based material. The emissions are centered at 450 nm and 420 nm for the $Cl^-$ and $Br^-$ analogues, respectively. Optical images of the samples under UV illumination are given in SI Figure S10. The excitation spectra of $Cs_2ZnCl_4$ highlights three clear maxima situated at ~370, 300, and 250 nm, whereas for $Cs_2ZnBr_4$, only one peak appears at 350 nm. There are limited data in the literature on the luminescence of $Cs_2ZnCl_4$ and essentially none apparent for $Cs_2ZnBr_4$. A prior report measured the luminescence spectrum of $Cs_2ZnCl_4$ single crystals; however, it yielded a photoluminescence emission maximum located at ~440 nm with an excitation spectrum somewhat different from the one reported herein, which yielded an analogous maximum situated at 450 nm.[7] This emission may be ascribed to either defects or impurities.

### 3.6.3. Spectroscopic Studies – Radioluminescence

The radioluminescence spectrum of $Cs_2ZnCl_4$ is shown in Figure 11A. The light output of $Cs_2ZnCl_4$ was estimated by comparison with a YAP: Ce powder standard. The measured intensity was determined to be ~1-2% of YAP: Ce or ~100-300 photons / MeV, which is comparable with the literature reported value for the corresponding single crystal.[6]

The RL spectrum of $Cs_2ZnCl_4$ is complex with at least 5 different contributions (situated at ~254, 305, 400, 500, and 760 nm, respectively) spanning over the entire investigated range. Moreover, the emission signals at 305 and 400 nm appear to comprise a composite nature. Some of these contributions are in rather good agreement with bulk literature results, particularly with respect to the features located at 254 nm and at the high energy side of the 305 nm peak.[5, 6] The prior cited references report three main emissions located at 3.3, 4.2, and 4.8 eV (i.e., 375, 295, and 258 nm, respectively), which have been attributed to an Auger-free luminescence (also known as cross-luminescence), due to transitions between the Cs 5*p* outermost core-band and the Cl 3*p*-based valence band. The presence of these bands suggests that our nanoscale samples also undergo the expected Auger-free luminescence phenomenon. Moreover, the broad shoulder at ~500 nm may be related to the PL emission, as it possesses a very similar emission shape, profile, and location to the emission signal reported in Figure S9C. Interestingly, an additional emission peak appears at 760 nm, which has not been previously noted before for $Cs_2ZnCl_4$. Future studies with extra, more judiciously chosen samples will enable us to more convincingly determine the exact nature of this peak.

The pulsed X-ray decay profile of $Cs_2ZnCl_4$ is reported in Figure 11C. The decay is very fast and can be described in terms of two exponential decays, i.e. decay times of the order of 2.6 and 8.6 ns, coupled with a much longer component, which appears as a constant fraction. The

fast decay component accounts for ~60 % of the total area, whereas the weight of the longer, slower component is ~30 % with the remainder assigned to the constant. We find that our experimental decay profile is in good agreement with that reported previously in the literature for $Cs_2ZnCl_4$. The faster decay times are also a characteristic of Auger-free luminescence (AFL), whereas the slower component suggests a non-AFL component.

Despite the lack of any RL signal from the $Cs_2ZnBr_4$ sample, pulsed X-ray measurements and RL intensity values have been reported on this system as well (Figure 11B, D). The data, reported for the sake of completeness, highlight a mostly very fast contribution, which is substantially indistinguishable from the measured pulse, and it is accompanied by much weaker signals with decay times of the order of few ns.

## 4. Conclusions

We have successfully generated and characterized not only (a) multiple types of unique nanoscale morphologies, including spheres, rods, and circular particles but also (b) three micron-scale particulate motifs, including plates, particles, and spindles, of $Cs_2ZnCl_4$ and $Cs_2ZnBr_4$. The techniques we have used have been focused on solution-based LARP and hot injection methods, which are generally milder and more cost effective as compared with conventional bulk methods, which have typically used to synthesize bulk crystals of these types of materials. We have investigated and correlated reaction temperature, surfactant, and time effects with nanoscale morphology using the hot injection method through a systematic variation of reaction conditions.

With respect to the hot injection method, our observations are consistent with a two-step growth mechanism, mediated by seed nucleation. We also highlight a correlation between reaction time and temperature in that both longer reaction times and higher reaction temperatures

appeared to result in the formation of larger rods. Conversely, lower reaction temperatures and shorter reaction times were more conducive to production of either square plates or particles. The effect of decreasing surfactant concentrations leads to the formation of square plates, whereas increasing surfactant amounts is more conducive to the analogous production of long ribbons of $Cs_2ZnCl_4$. Complementary XRF data have highlighted the relative uniformity of the elemental distribution within the as-prepared crystals, as expected.

A comparison table (Table 1) between the published data on $Cs_2ZnCl_4$ bulk and that of nanomaterials is provided below. We note that the RL data on bulk $Cs_2ZnBr_4$ was not reported, because of the lack of observed emission detected within the analogous nanorods; as such, we did not take these types of measurements on the bulk $Cs_2ZnBr_4$ sample. Nevertheless, preliminary optical PL studies of our nanoscale motifs have demonstrated differences from bulk behavior, including the presence of additional contributions that have not been previously reported. RL studies of $Cs_2ZnCl_4$ yielded a fast decay time and a low light output, that are comparable with what has been previously reported for the bulk. The main difference between our nanorod sample and that of the bulk is the addition of the 500 nm and 760 nm emission in the RL. In addition, PL spectra of our $Cs_2ZnCl_4$ sample showed an emission at maximum at 450 nm, whereas the bulk highlighted an emission at 440 nm, corresponding to a red shift of 10 nm.

Therefore, we are able to conclude the following from our findings. First, our as-prepared compounds do show promise as scintillators. Second, we have established synthetic means by which they can be reliably fabricated. Hence, the next step (and the subject of an extensive study) will be a much more systematic analysis in which we are able to correlate structural parameters, such as particle size and shape, with their corresponding scintillation properties.

## 5. Acknowledgements

This material is based on work supported by the Carol M. Baldwin Foundation for Breast Cancer Research. Structural characterization experiments (TEM and SEM) for this manuscript were performed in part at the Center for Functional Nanomaterials, located at Brookhaven National Laboratory, which is supported by the U.S. Department of Energy under Contract No. DE-SC-00112704. This research also used the Hard X-ray Nanoprobe Beamline at 3-ID of the National Synchrotron Light Source II, a U.S. Department of Energy (DOE) Office of Science User Facility operated for the DOE Office of Science by Brookhaven National Laboratory under Contract No. DE-SC0012704. The PL and RL studies were supported by the US Department of Energy/NNSA/DNN R&D and carried out at Lawrence Berkeley National Laboratory under contract No. AC02–05CH11231.

## References

1. J. M. Hall, S. Asztalos, P. Biltoft, J. Church, M. A. Descalle, T. Luu, D. Manatt, G. Mauger, E. Norman, D. Petersen, J. Pruet, S. Prussin and D. Slaughter, *Nuclear Instruments and Methods in Physics Research Section B: Beam Interactions with Materials and Atoms*, 2007, **261**, 337-340.
2. K. Watanabe, T. Yanagida, K. Fukuda, A. Koike, T. Aoki and A. Uritani, *Sensors and Materials*, 2015, **27**, 269-275.
3. V. Eijk and W. E. Carel, *Nuclear Instruments and Methods in Physics Research Section A: Accelerators, Spectrometers, Detectors and Associated Equipment*, 2003, **509**, 17-25.
4. T. Itoh, M. Kokubun, T. Takashima, T. Honda, K. Makishima, T. Tanaka, T. Yanagida, S. Hirakuri, R. Miyawaki, H. Takahashi, K. Nakazawa and T. Takahashi, *IEEE Transactions on Nuclear Science*, 2006, **53**, 2983-2990.
5. A. Ohnishi, M. Kitaura, M. Itoh and M. Sasaki, *Journal of the Physical Society of Japan*, 2012, **81**, 2118-2127.
6. N. Yahaba, M. Koshimizu, Y. Sun, T. Yanagida, Y. Fujimoto, R. Haruki, F. Nishikido, S. Kishimoto and K. Asai, *Applied Physics Express*, 2014, **7**.
7. K. Sugawara, M. Koshimizu, T. Yanagida, Y. Fujimoto, R. Haruki, F. Nishikido, S. Kishimoto and K. Asai, *Optical Materials*, 2015, **41**, 53-57.
8. P. A. Rodnyi, *Radiation Measurements*, 2004, **38**, 343-352.
9. S. A. Osseni, S. Lechevallier, M. Verelst, C. Dujardin, J. Dexpert-Ghys, D. Neumeyer, M. Leclercq, H. Baaziz, D. Cussac, V. Santran and R. Mauricot, *Journal of Materials Chemistry*, 2011, **21**.
10. R. Chouikrat, F. Baros, J. C. Andre, R. Vanderesse, B. Viana, A. L. Bulin, C. Dujardin, P. Arnoux, M. Verelst and C. Frochot, *Photochem Photobiol*, 2017, **93**, 1439-1448.
11. J. P. Scaffidi, M. K. Gregas, B. Lauly, Y. Zhang and T. Vo-Dinh, *ACS nano*, 2011, **5**, 4679-4687.
12. H. Chen, X. Sun, G. D. Wang, K. Nagata, Z. Hao, A. Wang, Z. Li, J. Xie and B. Shen, *Materials Horizons*, 2017, **4**, 1092-1101.
13. C. Zhang, K. Zhao, W. Bu, D. Ni, Y. Liu, J. Feng and J. Shi, *Angew Chem Int Ed Engl*, 2015, **54**, 1770-1774.
14. A. L. Bulin, A. Vasil'ev, A. Belsky, D. Amans, G. Ledoux and C. Dujardin, *Nanoscale*, 2015, **7**, 5744-5751.
15. P. Sengar, G. A. Hirata, M. H. Farias and F. Castillón, *Materials Research Bulletin*, 2016, **77**, 236-242.
16. B. Cline, I. Delahunty and J. Xie, *Wiley Interdiscip Rev Nanomed Nanobiotechnol*, 2019, **11**, e1541.
17. H. Chen, G. D. Wang, Y. J. Chuang, Z. Zhen, X. Chen, P. Biddinger, Z. Hao, F. Liu, B. Shen, Z. Pan and J. Xie, *Nano Lett*, 2015, **15**, 2249-2256.
18. N. Y. Morgan, G. Kramer-Marek, P. D. Smith, K. Camphausen and J. Capala, *Radiat Res*, 2009, **171**, 236-244.
19. D. R. Cooper, K. Kudinov, P. Tyagi, C. K. Hill, S. E. Bradforth and J. L. Nadeau, *Phys Chem Chem Phys*, 2014, **16**, 12441-12453.
20. Z. Du, X. Zhang, Z. Guo, J. Xie, X. Dong, S. Zhu, J. Du, Z. Gu and Y. Zhao, *Adv Mater*, 2018, **30**, e1804046.

21. A.-L. Bulin, C. Truillet, R. Chouikrat, F. Lux, C. Frochot, D. Amans, G. Ledoux, O. Tillement, P. Perriat, M. Barberi-Heyob and C. Dujardin, *The Journal of Physical Chemistry C*, 2013, **117**, 21583-21589.
22. P. Retif, S. Pinel, M. Toussaint, C. Frochot, R. Chouikrat, T. Bastogne and M. Barberi-Heyob, *Theranostics*, 2015, **5**, 1030-1044.
23. A. G. Ostrogorsky, V. Riabov and N. Dropka, *Journal of Crystal Growth*, 2018, **498**, 269-276.
24. A. R. Lim, O. H. Han and S.-Y. Jeong, *Journal of Physics and Chemistry*, 2003, **64**, 933-937.
25. A. R. Lim, *Journal of Applied Physics*, 2010, **107**, 1-6.
26. M. Senthil Pandian, K. Boopathi, P. Ramasamy and G. Bhagavannarayana, *Materials Research Bulletin*, 2012, **47**, 826-835.
27. M. J. Weber, *Journal of Luminescence*, 2002, **100**, 35-45.
28. A. Pan, B. He, X. Fan, Z. Liu, J. J. Urban, A. P. Alivisatos, L. He and Y. Liu, *ACS Nano*, 2016, **10**, 7943-7954.
29. Q. Chen, J. Wu, X. Ou, B. Huang, J. Almutlaq, A. A. Zhumekenov, X. Guan, S. Han, L. Liang, Z. Yi, J. Li, X. Xie, Y. Wang, Y. Li, D. Fan, D. B. L. Teh, A. H. All, O. F. Mohammed, O. M. Bakr, T. Wu, M. Bettinelli, H. Yang, W. Huang and X. Liu, *Nature*, 2018, **561**, 88-93.
30. J. Chattopadhyay, F. de Jesus Cortez, S. Chakraborty, N. K. H. Slater and W. E. Billups, *Chemistry of Materials*, 2006, **18**, 5864-5868.
31. Y. Yin and A. P. Alivisatos, *Nature*, 2005, **437**, 664-670.
32. C. R. Bealing, W. J. Baumgardner, J. J. Choi, T. Hanrath and R. G. Hennig, *ACS Nano*, 2012, **6**.
33. N. Pradhan, D. Reifsnyder, R. Xie, J. Aldana and X. Peng, *J. Am. Chem. Soc.*, 2007, **129**, 9500-9509.
34. A. Monshi, M. R. Foroughi and M. R. Monshi, *World Journal of Nano Science and Engineering*, 2012, **2**, 154-160.
35. J. Zhang, Q. Wang, X. Zhang, J. Jiang, Z. Gao, Z. Jin and S. Liu, *RSC Advances*, 2017, **7**, 36722-36727.
36. T. Udayabhaskararao, M. Kazes, L. Houben, H. Lin and D. Oron, *Chemistry of Materials*, 2017, **29**, 1302-1308.
37. R. S. Ningthoujam, A. Gautam and N. Padma, *Phys Chem Chem Phys*, 2017, **19**, 2294-2303.
38. Y. Bekenstein, B. A. Koscher, S. W Eaton, P. Yang and A. P. Alivisatos, *J Am Chem Soc*, 2015, **137**, 16008-16011.
39. F. Zhang, H. Zhong, C. Chen, X.-G. Wu, X. Hu, H. Huang, J. Han, B. Zou and Y. Dong, *ACS nano*, 2015, **9**, 4533-4542.
40. J. A. McGinnety, *Inorganic Chemistry*, 1974, **13**, 1057-1061.

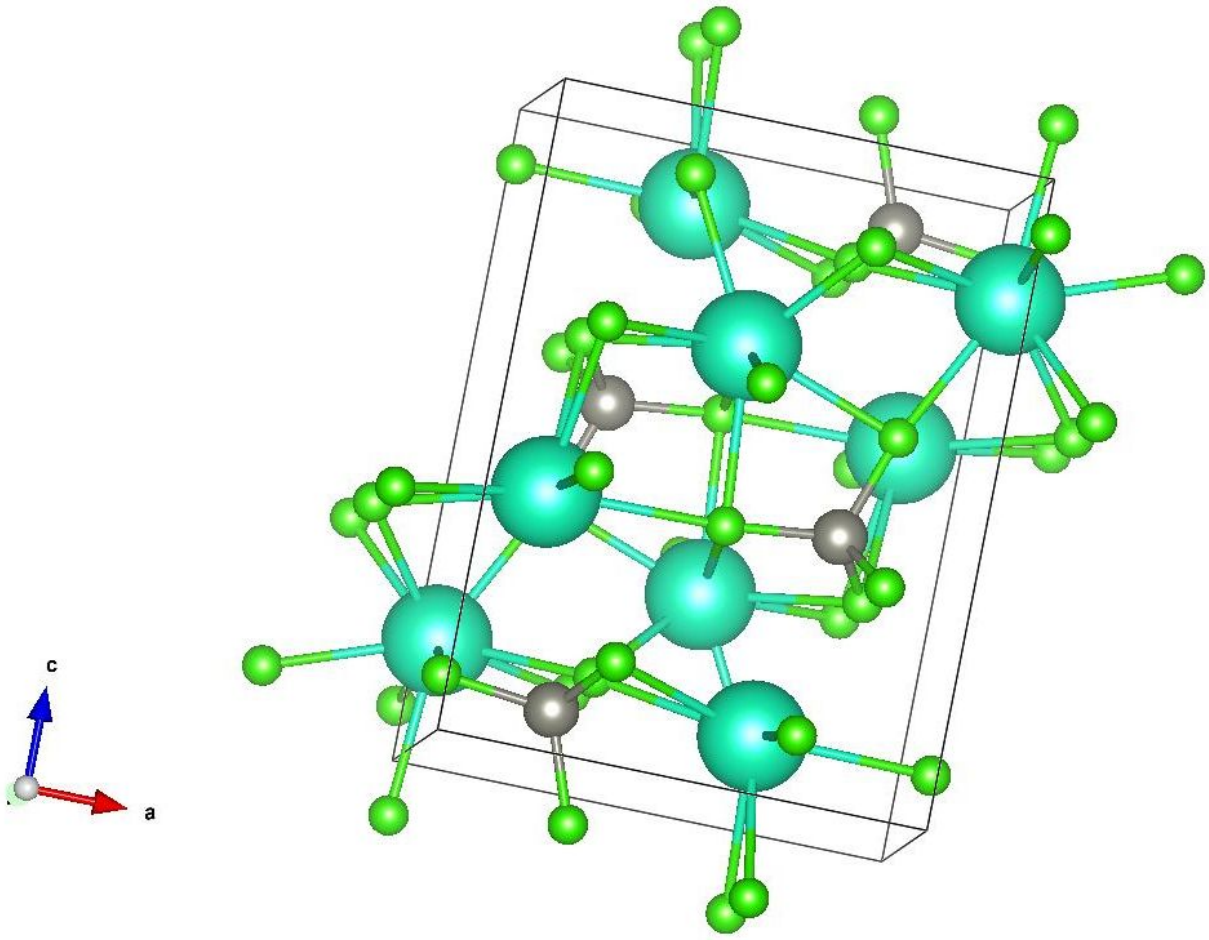


**Figure 1.** 'Ball-and-stick' schematic of $Cs_2ZnCl_4$. Zinc (grey), cesium (teal), and chlorine (green) are highlighted.

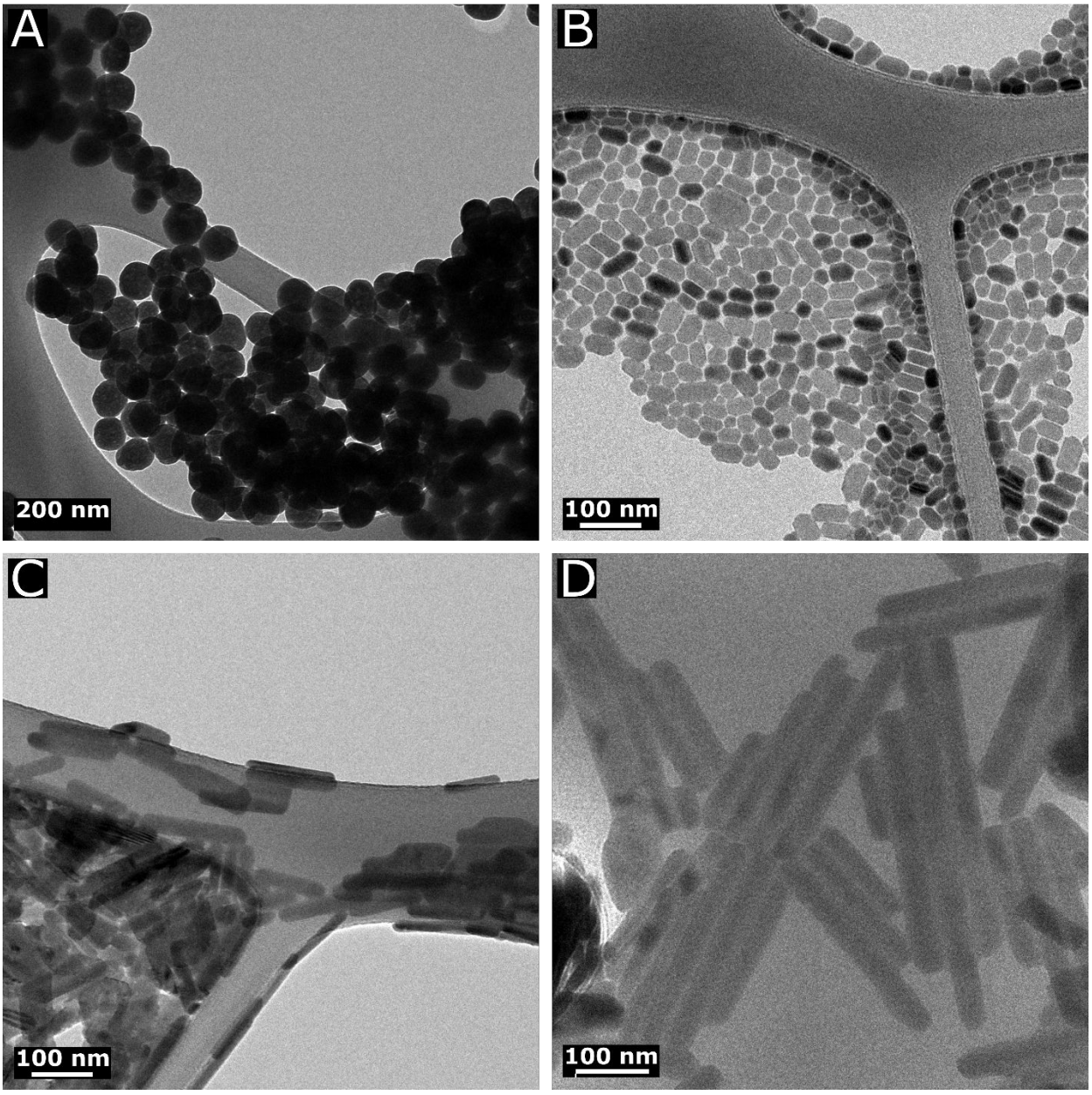


**Figure 2.** Hot injection method. Morphology of $Cs_2ZnCl_4$ prepared at different reaction temperatures. The reaction time was kept constant at 20 minutes in the presence of surfactants in a 1:1 molar ratio of oleic acid and oleylamine. We were able to isolate (A) nanospheres at 50°C, (B) acicular nanoparticles at 100°C, (C) monodisperse, smaller-diameter nanorods at 150°C, and (D) larger, more polydisperse nanorods at 200°C.

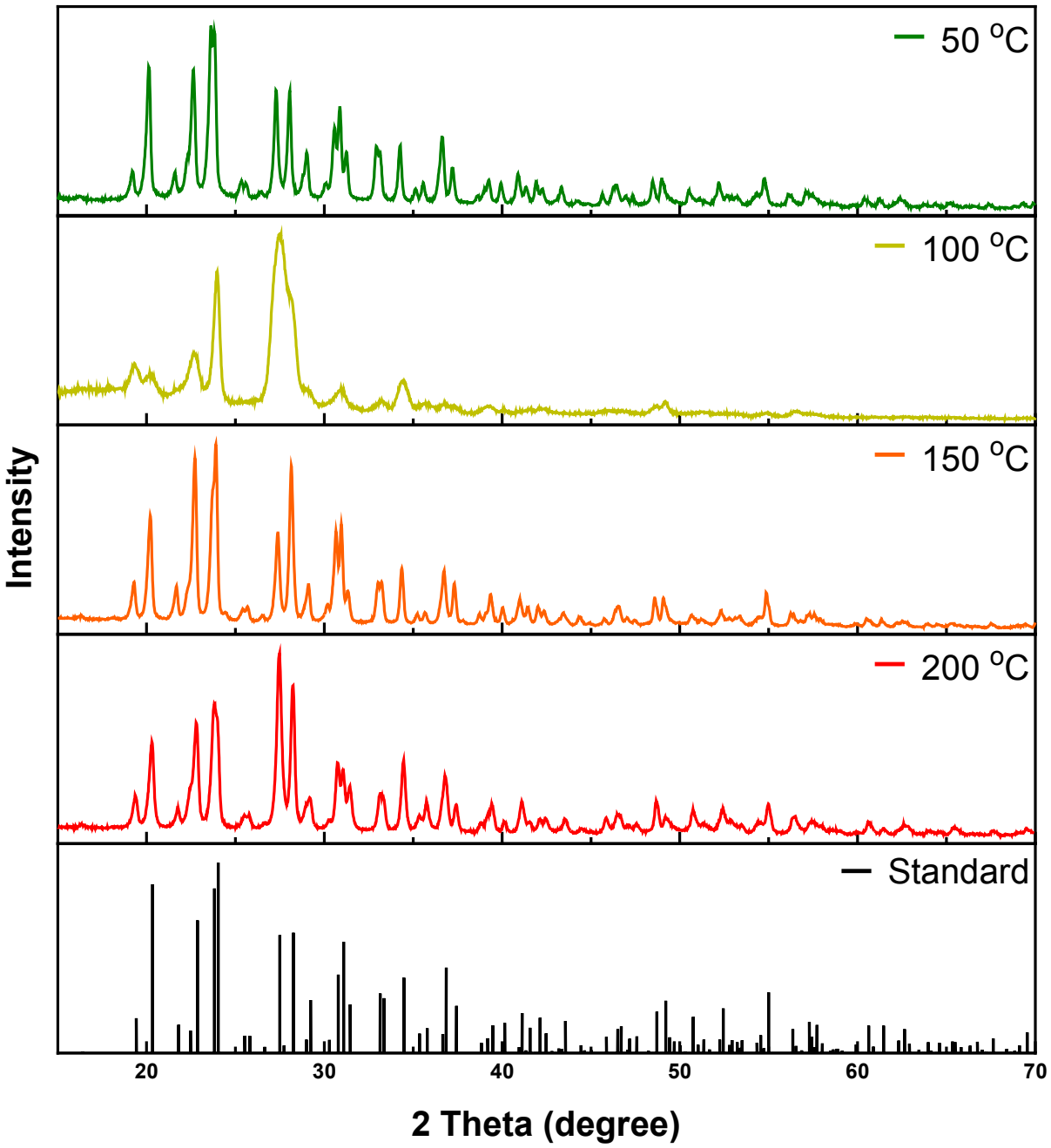


**Figure 3.** Hot Injection Method. *Probing the effect of reaction temperature on $Cs_2ZnCl_4$.* XRD patterns for samples, prepared at 50°C (green), 100°C (yellow), 150°C (orange), and 200°C (red), respectively. All experimental data are compared with the published standard pattern for $Cs_2ZnCl_4$ (black)[40].

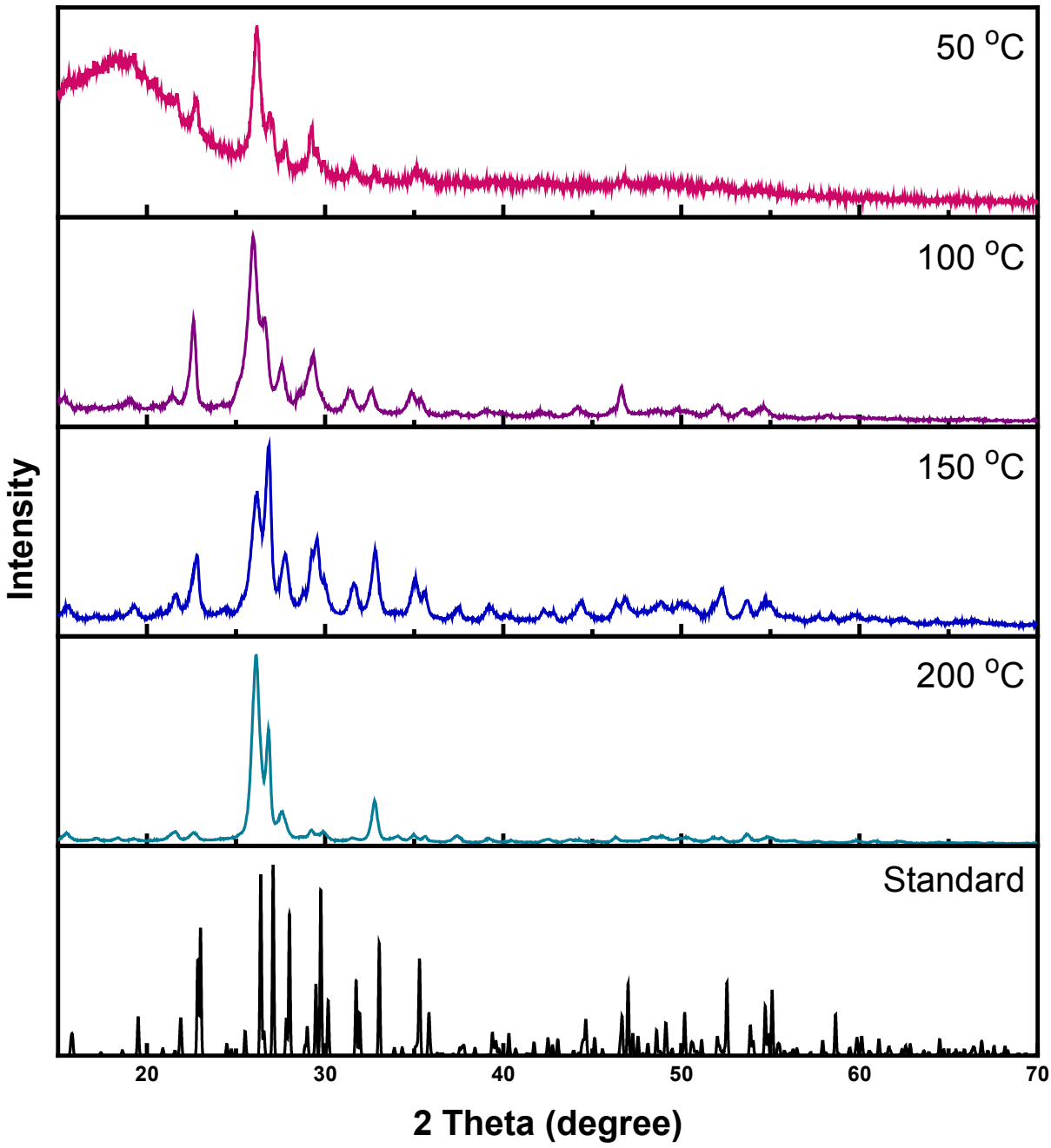


**Figure 4.** Hot Injection Method. *Probing the effect of reaction temperature on $Cs_2ZnBr_4$.* XRD patterns for samples, prepared at 50°C (pink), 100°C (purple), 150°C (blue), and 200°C (teal), respectively. All experimental data have been compared with the published standard pattern for $Cs_2ZnCl_4$ (black).[40]

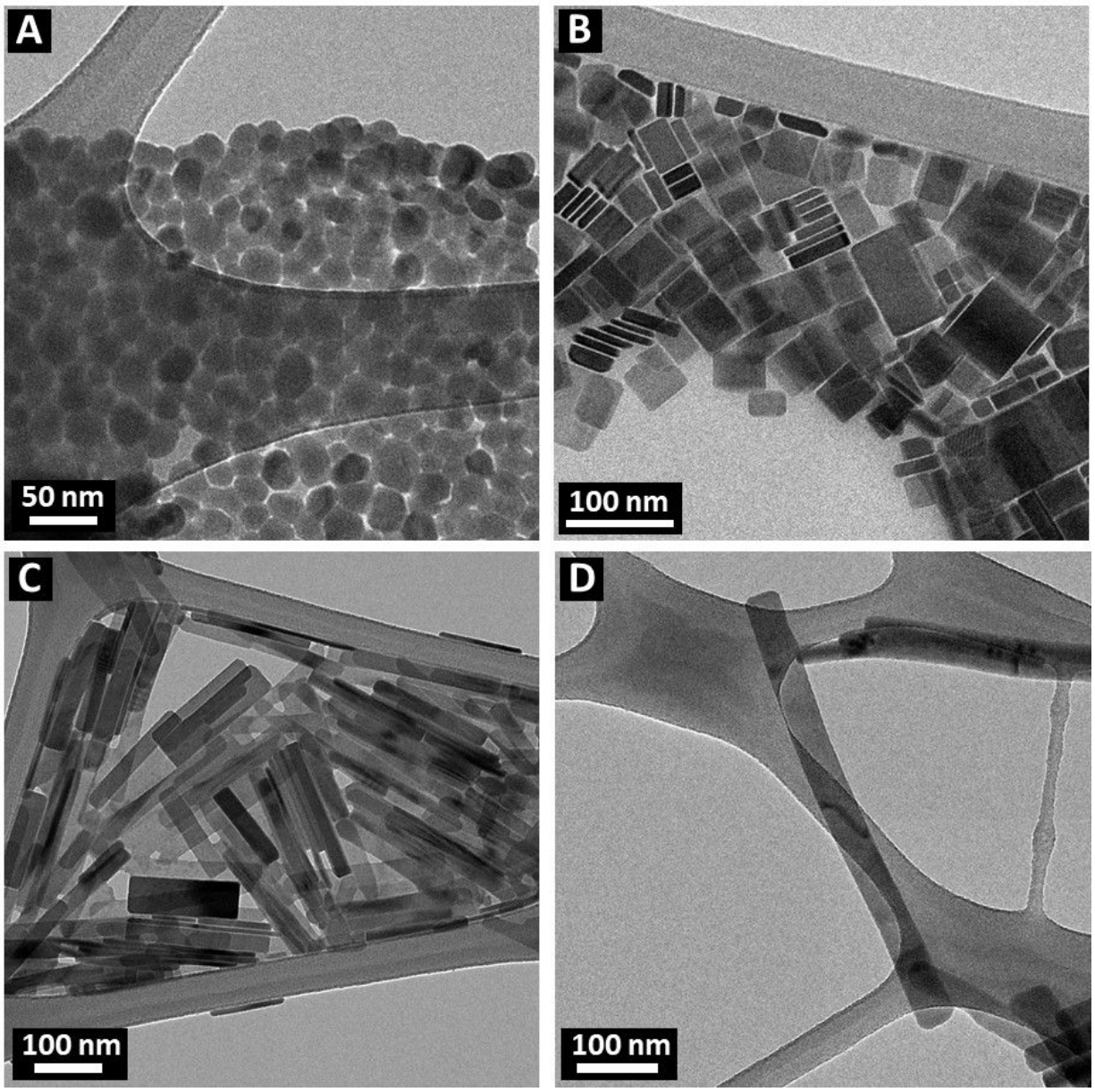


**Figure 5.** Hot injection method. Morphology of $Cs_2ZnBr_4$ prepared at different temperatures. The reaction time was kept constant at 20 minutes in the presence of surfactants using a 1:1 molar ratio of oleic acid and oleylamine. We were able to isolate (A) acicular particles at 50°C, (B) square plates at 100°C, (C) monodisperse, flattened nanorods at 150°C, and (D) large, more polydisperse flattened nanorods at 200°C.

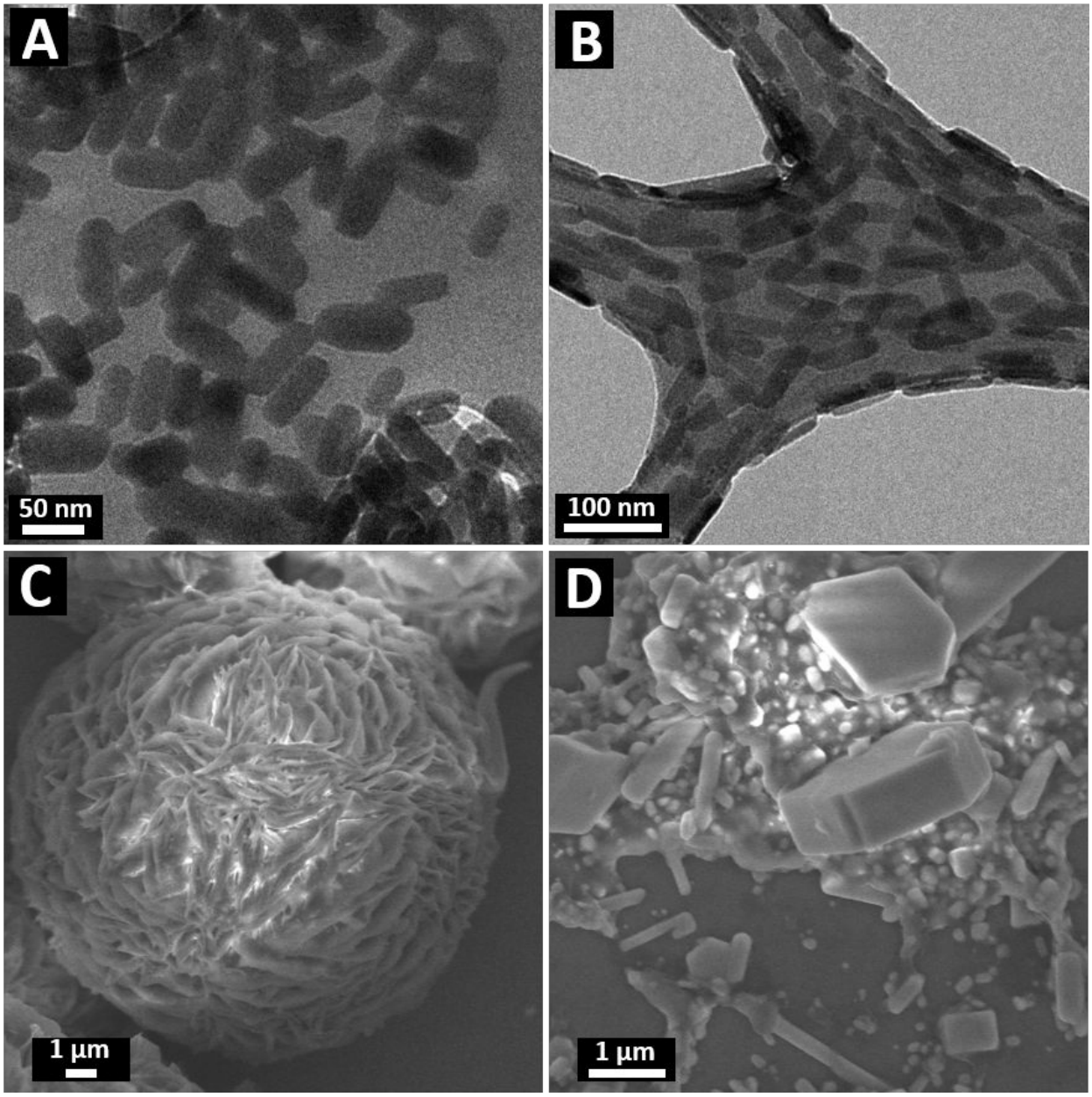


**Figure 6.** Hot Injection Method. *Effect of surfactant*. TEM images of reactions run at 150°C, using (A) nonylamine, instead of oleylamine, and (B) dodecanoic acid, instead of oleic acid. (C) corresponds to an OLA-free reaction, whereas (D) is associated with an OA-free reaction.

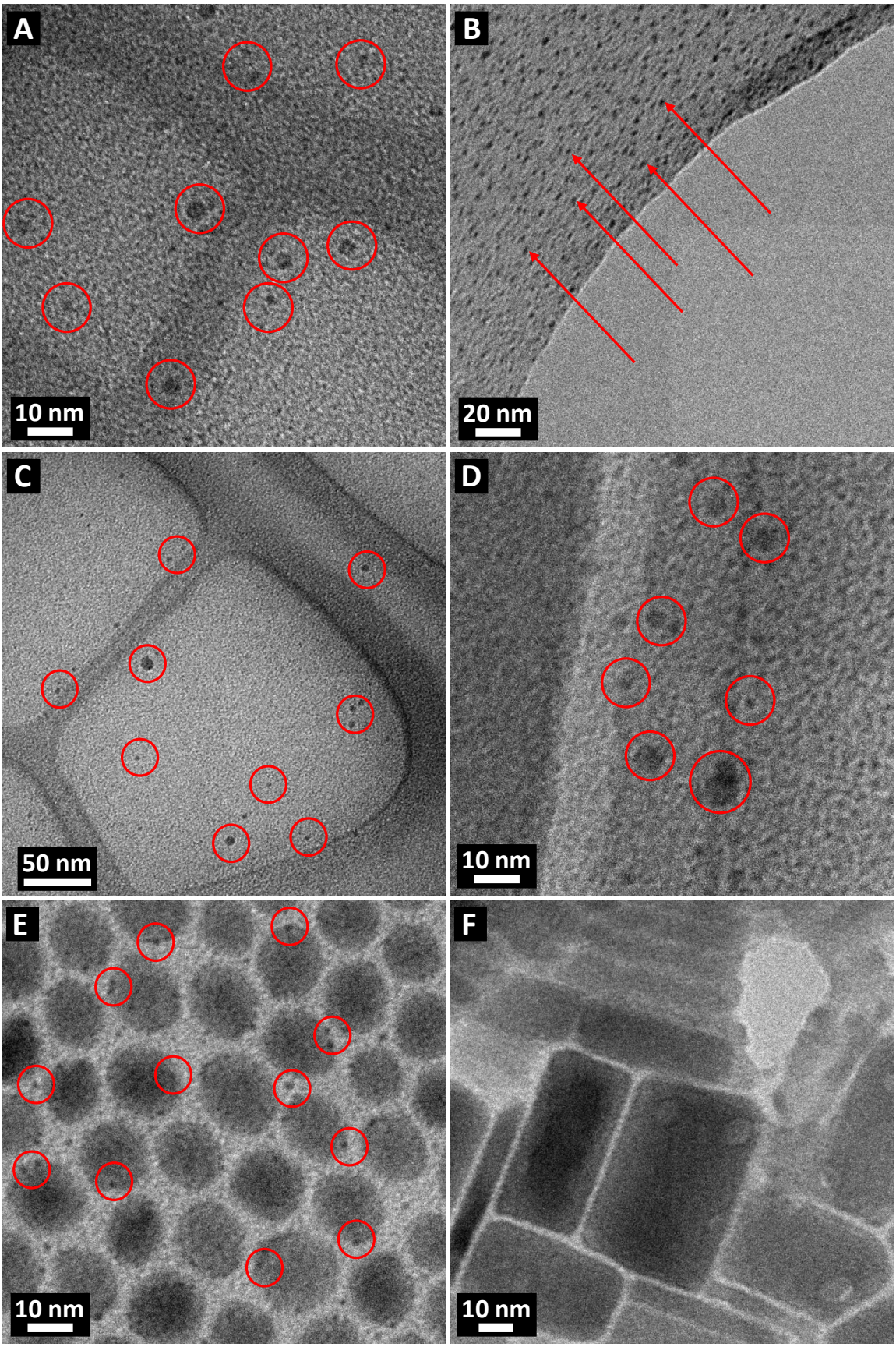
A
10 nm
B
20 nm
C
50 nm
D
10 nm
E
10 nm
F
10 nm

**Figure 7.** Mechanistic Insights into Hot Injection. TEM images of zinc seeds obtained before injection of Cs-OA when (A) $ZnCl_2$ and (B) $ZnBr_2$ are used. Seed particles for chloride (C) and bromide (D) analogues from supernatant solution, after injection of the Cs-OA and subsequent centrifugation. (E) highlights $Cs_2ZnCl_4$ created immediately after Cs-OA addition with clearly visible seed particles. (F) presents $Cs_2ZnBr_4$ with no visible seed particles. Seed particles are either circled in red or indicated by red arrows.

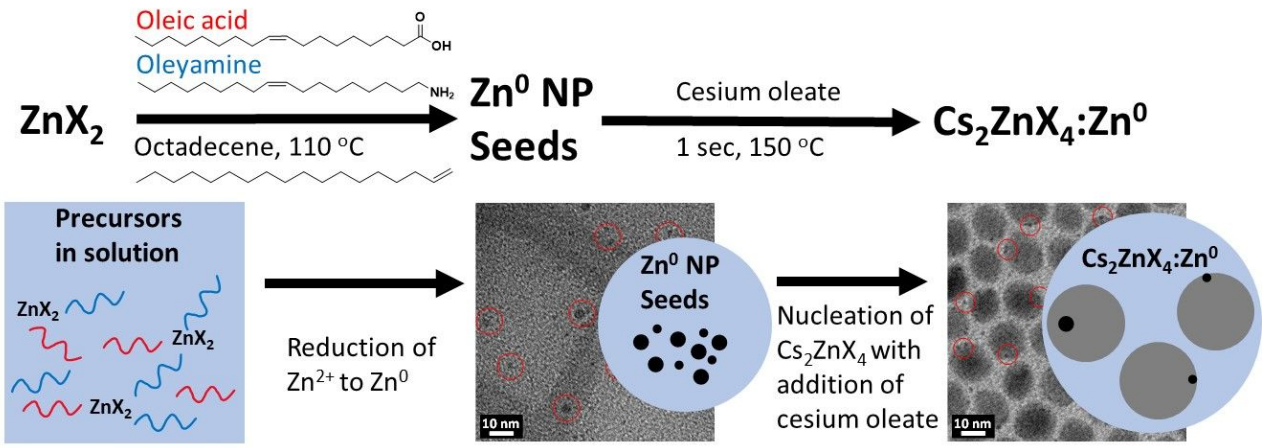


**Figure 8.** Proposed mechanistic flow-chart, associated with the various stages underlying the seed-mediated growth of $Cs_2ZnX_4$ nanocrystals.

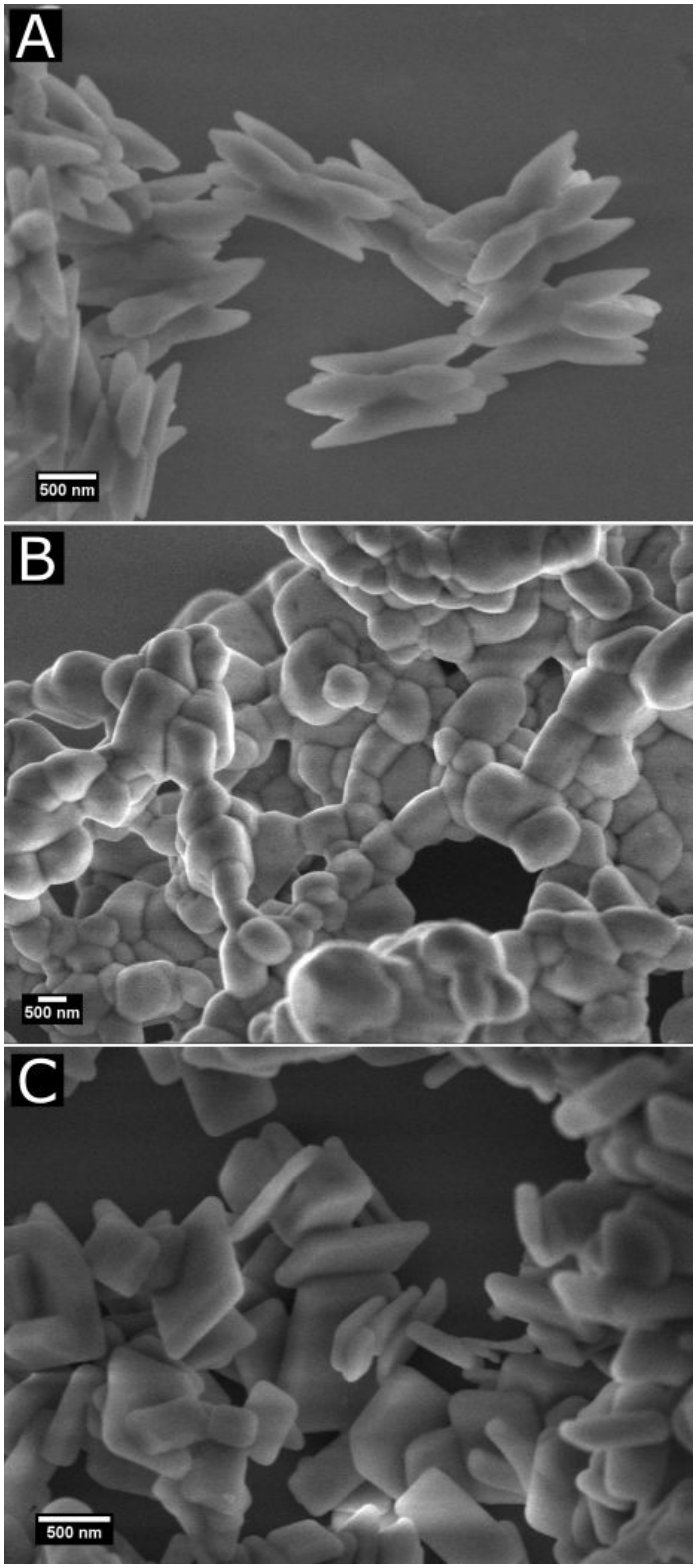


**Figure 9.** LARP method. SEM images of micron-scale particles, including (A) spindles of $Cs_2ZnCl_4$, (B) particulate motifs of $Cs_2ZnCl_4$, and (C) rectangular plates of $Cs_2ZnBr_4$.

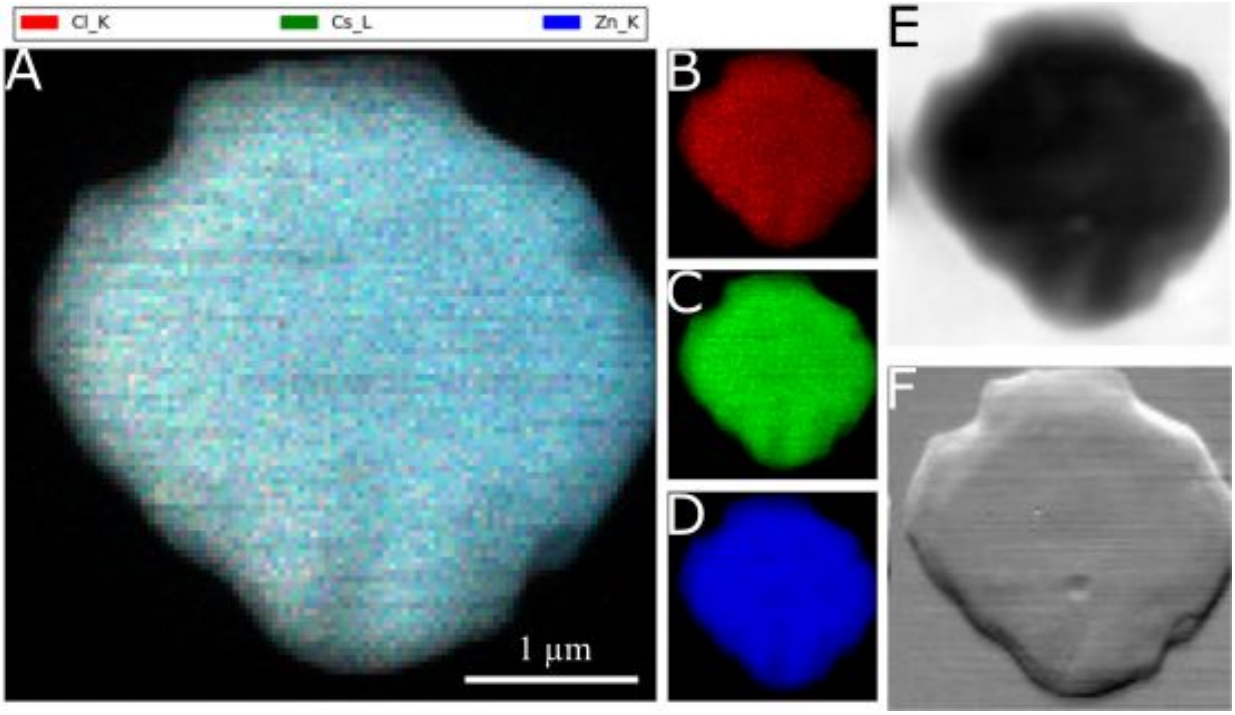


**Figure 10.** (A) XRF elemental map of $Cs_2ZnCl_4$. Elemental distributions within the analyzed particle of (B) chlorine (red); (C) cesium (green); and (D) zinc (blue), respectively. Corresponding (E) phase contrast and (F) differential phase contrast (DPC) images are also shown.

| Material | Measured Size | Image | RL Emission Peak Positions (nm) | RL decay (ns) | PL Emission Peak Positions (nm) | PL Decay (ns) | Reference |
|---|---|---|---|---|---|---|---|
| $Cs_2ZnCl_4$ nanorods | 101.3 ± 24.4 nm | See Figure 2C | 254, 305, 400, 500, & 760 | 2.6 | 450 | 3.6 | This work |
| $Cs_2ZnBr_4$ nanorods | 206 ± 50 nm | See Figure 5C | No emission | Indistin-guishable from the pulse | 420 | 2.4 | This work |
| $Cs_2ZnCl_4$ bulk | bulk | See ref. 5 | 258, 295, & 375 | 1.6 | 440 | Not reported | 5 |

**Table 1.** Comparison between measured RL and PL data of as-synthesized nanorods versus published bulk values.

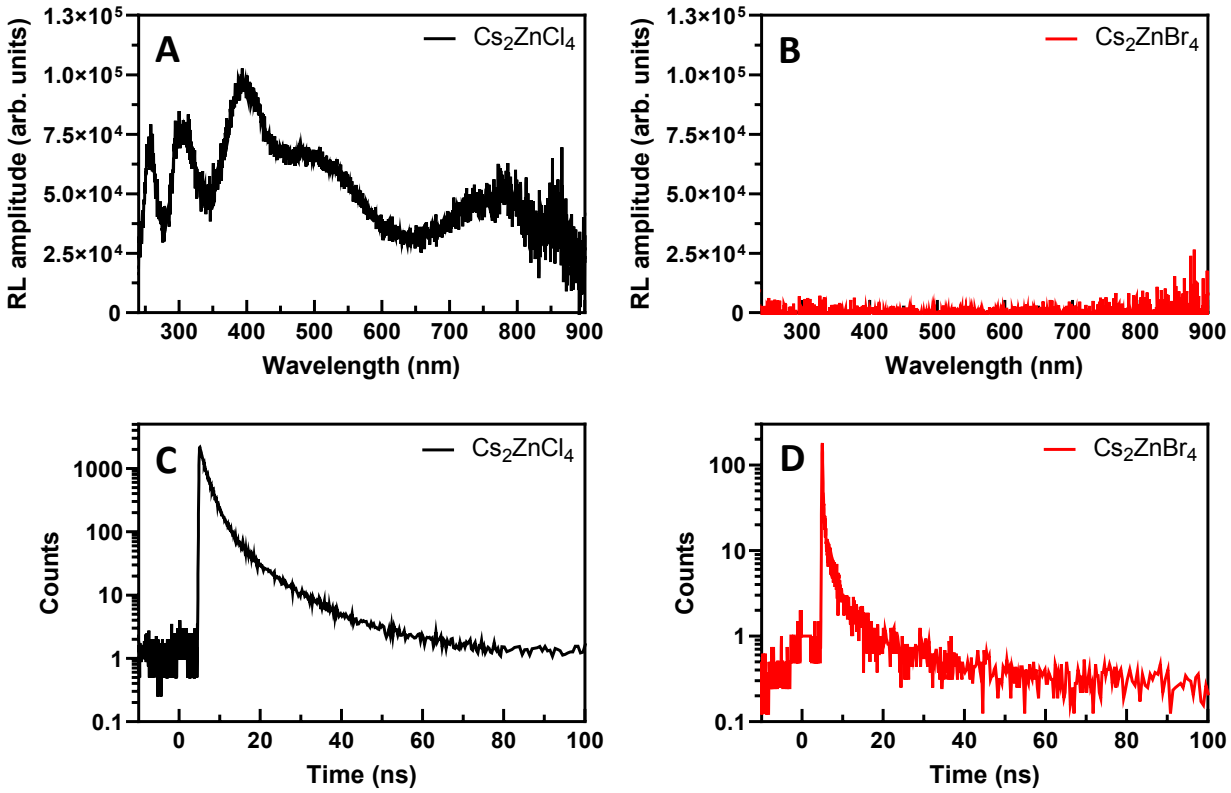


**Figure 11.** Room temperature RL spectrum of (A) $Cs_2ZnCl_4$ and (B) $Cs_2ZnBr_4$. Pulsed X-ray decay profiles were obtained on (C) $Cs_2ZnCl_4$ and (D) $Cs_2ZnBr_4$.